Georgieva et al. Journal of the European Optical Society-Rapid Publications (2020) 16:7
https://doi.org/10.1186/s41476-020-00129-4

Journal of the European Optical Society-Rapid Publications

RESEARCH Open Access

Design and performance analysis of integrated focusing grating couplers for the transverse-magnetic TM_{00} mode in a photonic BiCMOS technology

Galina Georgieva[1*], Karsten Voigt[1], Anna Peczek[2], Christian Mai[3] and Lars Zimmermann[1,3]

Abstract

Focusing grating couplers for the excitation of the fundamental transverse-magnetic (TM) mode in integrated silicon photonic waveguides are designed and characterized under the boundary conditions of a photonic BiCMOS foundry. Two types of waveguide geometries are considered – a nanowire and a rib waveguide. Wafer-scale experimental results for nanowire TM grating couplers are in excellent agreement with numerical investigations and demonstrate a robust behavior on the wafer. The mean coupling loss and the 3σ interval are -3.9 ± 0.3 dB. The on wafer variation is three times lower than for the fundamental transverse-electric (TE) polarization. Similarly, the coupling in rib waveguides is examined as well. The results indicate that the rib waveguides require a modified geometry when designed for TM. In general, the nanowire waveguide type is more suitable for TM coupling, showing a stable and repeatable performance.

Keywords: Photonic integration, Integrated waveguides, Silicon nanowire, Silicon rib waveguide, Transverse-magnetic mode, Focusing grating coupler, Integrated grating coupler, Photonic BiCMOS

Introduction

Over the recent years, integrated optical communication systems are gaining in importance and are receiving a strong interest from both industry and research. For their accomplishment, silicon photonics offers the possibility of the integration of optics in parallel with electronics on existing CMOS or BiCMOS platforms [1, 2]. The most important property of silicon photonic waveguides is the high index contrast between Si as a core and SiO_2 as a cladding. With this, light can be guided in waveguides with very small dimensions, which allows for a high-density integration and a large-scale fabrication. On the other hand, the high index contrast inevitably leads to a strong birefringence – the fundamental transverse-electric (TE) and transverse-magnetic (TM) polarizations have a large difference in their effective refractive indices and consequently, all silicon photonic components are strongly polarization dependent [3]. For the main application of silicon photonics for optical communications, the typical components are well studied and an operation with the TE_{00} mode has been established as a standard.

When moving away from the classical applications of silicon photonics, the adoption of TM becomes again interesting. Trends from the recent few years show an increasing number of developments in the area of sensing and biosensing, where the strong evanescent field component of TM is of great advantage [4–7]. Furthermore, highly stable frequency comb generation can be supported by TM, as shown in [8]. Signal regeneration enabled by four-wave-mixing (FWM) involving the TM mode was demonstrated in a single-mode regime [9]

* Correspondence: galina.georgieva@tu-berlin.de
[1]Technische Universität Berlin, Office HFT 4, Einsteinufer 25, 10587 Berlin, Germany
Full list of author information is available at the end of the article

and more recently, intermodal FWM [10] allowed for a large wavelength conversion. Novel on-chip components like optical isolators and circulators [11] require an operation with the TM polarization as well.

Independent of the application field, the coupling problem is always present in silicon photonics. Because of the large mode mismatch between the silicon waveguide and external light sources like single-mode-fibers (SMF), light coupling on chip is one of the most challenging issues. A possible solution is the design of grating couplers (GCs), in which the silicon waveguide is tapered to match the dimensions of the SMF and then periodically etched to direct the light to the fiber by diffraction. Having been more important so far, the TE_{00} mode coupling received more attention and a huge variety of grating couplers for TE is available. On the other hand, grating couplers for TM_{00} are reported seldom. In linear GCs [12], the TM_{00} mode passes through a long taper, where a mode hybridization takes place [13]. To avoid this effect, focusing GCs (FGCs) need to be designed instead, which also have the obvious advantage of having a reduced on-chip footprint. There were several successful demonstrations of FGCs for TM in the past. For nanophotonics, uniform [14] and apodized [15] subwavelength designs show a good performance with a coupling loss of − 3.7 dB and − 3.3 dB respectively. FGC for TM with subwavelength teeth reducing the Fresnel reflection and achieving − 5 dB loss were reported as well [16]. A TM FGC for silicon-organic-hybrid applications with a coupling loss of − 3.95 dB was shown in [17]. The reported designs require, however, non-standard fabrication techniques like electron beam lithography or the application of polymer cladding.

A natural next step would be to move to fully integrated devices, offering a large-scale fabrication and considering the limitations of the foundry used. Here, we propose designs for TM FGCs that take into account the integration boundary conditions of a photonic BiCMOS [18]. The designs include GCs for nanowire (short: wire TM FGC) and shallowly or deeply etched rib waveguides (short s-rib TM FGC and d-rib TM FGC). Rib waveguides are especially important for non-linear applications on silicon, where a lateral pin diode is necessary to reduce the free-carrier absorption loss [19]. Furthermore, recent reports show that MOS capacitor modulators comprising rib waveguides have a better modulation performance when operating with TM [20, 21].

Previously [22], we described the numerical design procedure for wire TM FGCs in a photonic BiCMOS technology and verified its reliability by manual on-chip measurements. We obtained a moderate coupling loss of − 4.3 dB, which was in a good agreement with the simulations. A manual measurement is sufficient to control the simulation results, but is still not a thorough characterization under the foundry boundary conditions. Therefore, we extend here our work by full-wafer measurements, in order to proof statistically the compatibility of the proposed TM FGCs with the photonic BiCMOS limitations. We demonstrate highly robust wire TM FGC designs, which are less sensitive to fabrication variations in comparison to their TE counterparts.

In the case of rib TM FGCs designs, we face additional issues, which do not necessarily address to the grating couplers themselves. We explain the effects occurring in their case and discuss solutions, which still make it possible to use TM on rib waveguides.

Methods

In this section, we first describe the specifics of the photonic BiCMOS technology that need to be considered and our numerical design approach. Afterwards, details on the experimental setup and the measurement procedure are provided as well.

Photonic BiCMOS platform

Monolithic photonic-electronic integration has certain advantages compared to a separate integration, which are illustrated in the following example of a photonic BiCMOS platform [18]. Here, fast SiGe: C heterojunction bipolar transistors (HBT) are realized in the front-end of line (FEOL) in parallel with silicon-on-insulator (SOI) photonic components, including waveguides, modulators, grating couplers and photodiodes. Both electronics and photonics are covered by a backend of line (BEOL) stack, which comprises multiple SiO_2 and Si_3N_4 layers with different properties and thicknesses (Fig. 1). Using the metals in the backend of line, the shortest interconnects between photonics and electronics can be realized, which minimizes parasitic effects and allows for the accomplishment of high-speed systems. A disadvantage of such systems is the limited space for optimization of the photonic components, which often have individual requirements. The main limitations in our photonic BiCMOS platform for the grating couplers are: (a) fixed feature-size resolution, because of the 248 nm deep UV lithography used, (b) fixed backend of line stack height, layer thicknesses and material composition. Top and bottom layer thicknesses are shown to be crucial for the GC performance [23].

Numerical design

We follow the design workflow described in more detail in [22] and consider similarly the case of an out-coupling GC. For any type of grating coupler, the basic modeling steps remain the same. To determine a desired coupling angle ϑ, the effective refractive index n_{eff} of the grating area must be known. The latter depends on the grating slot width w_{slot} (the width of the etched part) and the etch

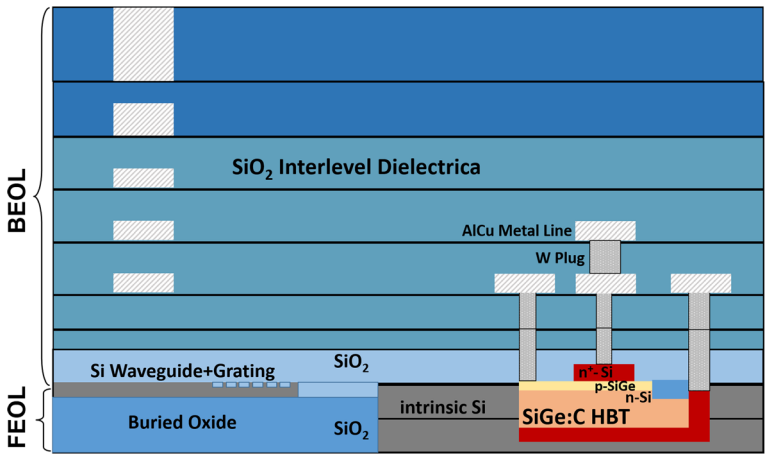

Fig. 1 Example of a photonic BiCMOS platform in cross-section. Electronics (e.g. heterojunction bipolar transistors, HBT) in bulk-Si depicted on the right hand side are integrated in parallel with silicon-on-insulator (SOI) photonic components in the frontend of line (FEOL). Both are covered by a complex backend of line (BEOL) stack, here represented in a simplified form

depth d, which are varied during the optimization process to maximize the out-coupled power. To keep the coupling angle ϑ constant, the grating period Λ must be adjusted according to the effective refractive index change.

Additional improvement of the GC efficiency can be achieved by choosing an appropriate buried-oxide (BOX) thickness or top layer thickness. When we work with integrated grating couplers, the following constraints occur:

- The material composition of the waveguide is more complex; therefore, known simple analytical methods like averaging the effective indices of the etched and non-etched grating area cannot be used to determine accurately the effective refractive index, when the grating slots dimensions are changed (cf. [24]).
- The BOX and top layer thicknesses are fixed and cannot be varied for an additional GC improvement.

The latter problem means that we have less flexibility for our design optimization and the choice of an appropriate coupling angle can be important as well, in order to ensure a constructive superposition of the waves diffracted upwards and reflected by the substrate. To handle the first problem, the effective refractive index n_{eff} is estimated after every optimization step, by using a spatial Fourier transform for the calculation of the real radiation angle. The technique is inspired by the antenna theory; a concept for the estimation of the radiation angles from the near field distribution was first proposed in [25]. Once the radiation angle ϑ is estimated, the actual n_{eff} can be derived by its usual relation to the angle ϑ and the grating period Λ. If necessary, the period can be afterwards adjusted for a desired coupling angle ϑ without changing the slot dimensions corresponding to n_{eff}.

Grating period and coupling angle are related to each other by a well-known formula for the diffraction condition for curved gratings [26], which is here written in polar coordinates, according to Fig. 2.

$$n_{eff} - \frac{m\lambda}{\rho_m} = \cos\gamma \sin\vartheta, \quad m \in \mathbb{N}\setminus\{0\} \tag{1}$$

Here, n_{eff} is the effective refractive index in the grating area, 2γ is the taper opening angle, λ is the design wavelength, ϑ is the coupling angle and ρ_m give the positions of discrete radii, which define the positions of the grating slots with increasing number m. The grating period Λ hides in the formula as the difference between two neighboring radii.

Because n_{eff} is estimated with the help of numerical simulations, its accuracy is limited by the numerical accuracy of the angle ϑ. The numerically predicted angles have a limited precision, because of the possible impact of the perfectly matched layers (PML) used to represent an open boundary condition, in combination with dispersive materials. In such cases, a numerical reflection is inevitable. For more details on this issue, please refer e.g. to [27].

Figure 2 shows further the models for a nanowire and rib waveguide FGCs. A separate model for the rib waveguide is necessary, as rib waveguides have larger effective refractive indices than nanowires and another type of backend stack covering, which also differs for shallowly and deeply etched ribs.

The taper start width is 500 nm, the end width is 19.25 μm with a total length of 39.6 μm. The dimensions correspond to a taper opening angle of $2\gamma = 28°$. The first

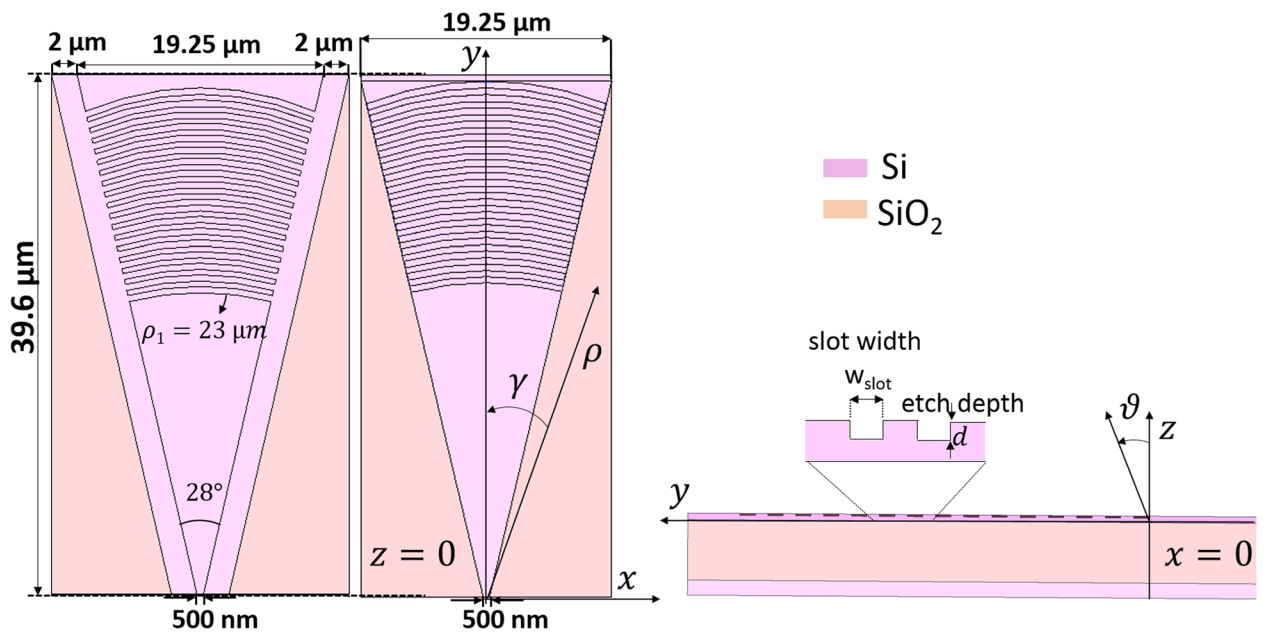

Fig. 2 Numerical models of focusing TM GCs for rib (left) and a nanowire (right) waveguides, including the taper geometry. Grating parameters for optimization are the slot width w_{slot} and the etch depth d

grating period is defined at ρ_1= 23 µm, where the taper width is about 10 µm and is enough for a good overlap with an SMF mode. An example of the three waveguide types and their transverse magnetic field distribution is given in Fig. 3. For all models, the BOX thickness is 2 µm and the Si waveguide height is 220 nm. The slab height of the rib waveguide is 150 nm for the shallowly etched or 100 nm for the deeply etched one.

A commercial finite-integration-technique [28] implemented in the time domain solver by Simulia CST is used for full 3D numerical simulations. The design wavelength in all cases is 1550 nm; the simulation wavelength range is from 1500 nm to 1600 nm. A resolution of 15 grid cells per minimal wavelength was found to be appropriate. A numerical reflection level at the PML of below 10^{-6} was enforced. The choice of these settings is empirically approved and leads to a deviation between measured and simulated angles of no more than 2°. Such difference is typical when fabrication deviations of the waveguide height, the grating slot dimensions or the top or bottom layers are present.

For the wire TM FGCs, structures for two different coupling angles centered at 1550 nm are designed. For

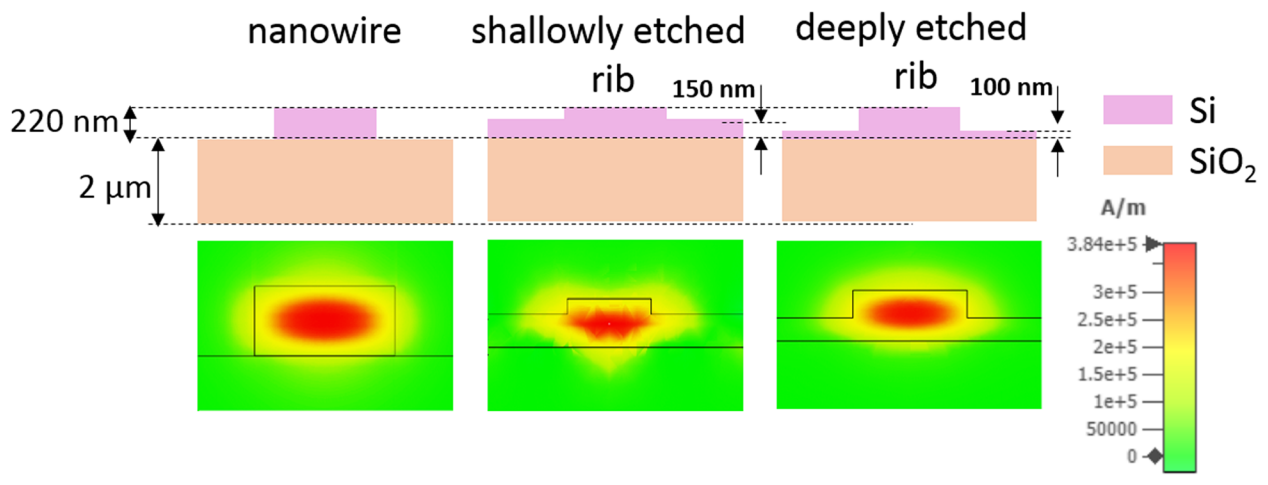

Fig. 3 Example of different types of silicon waveguides considered for the TM FGC design. The nanowire and rib widths are 500 nm. Below: mode field distribution of the transverse magnetic field component

the rib TM FGCs, a single coupling angle is chosen and the designs with different slab heights are studied.

Experimental devices and setup

Test devices for back-to-back measurements are fabricated on 200 mm wafers under a full photonic BiCMOS flow. The characterization involves two different test fields. Schematic of the fabricated devices can be seen in the Fig. 4 (a), where the structure on the left hand side is used in the first test field (test field 1) and the structure on the right hand side – in the second test field (test field 2).

On the first test field, we have 91 chips, which include a wire TM FGC and a reference TE FGC with standard dimensions (610 nm period, 317 nm slot width, 70 nm etch depth) for a direct comparison with the TM FGC in terms of coupling loss and 3σ variation on the wafer. The back-to-back structure for both TM and TE consists of two 1D GCs as in- and output, connected by a waveguide of 870 μm length with negligible loss (for TM ~ 1.5 dB/cm, for TE ~ 2 dB/cm), which is therefore not taken into account. The waveguide includes an S-bend for filtering of possible higher order modes.

On the second test field, we have 61 chips containing a second wire TM FGC design. For this structure, slot width variations are defined, in order to investigate their impact on the coupling loss and the 3σ variation. Their values are chosen to be significantly larger than process variations permitted by the foundry. In addition, the wire TM FGCs on the second test field can be compared with the wire TM FGC on the first test field in terms of 3σ variation. They are designed to have a large difference in their grating period, resp. central wavelength for that purpose. More details on the concrete designs follow in the next section.

Test field 2 includes further the two types of rib TM FGCs and reference rib TE FGCs with the same geometry as the reference nanowire TE FGC. The second test field allows for a direct comparison of the coupling loss and the 3σ variation of the three types of TM FGCs (designed for nanowire, shallowly and deeply etched rib waveguides).

The connecting waveguides for all structures on the second test field are this time 250 μm long, without an S-bend.

For our back-to-back measurements, we entirely rely on an automatic wafer-probe system. We use a tunable laser source Keysight 81608A, followed by a manual polarization controller and the device under test (DUT). After light in- and out-coupling with cleaved standard SMFs, the power is detected by an optical power meter Keysight M7745A. A schematic setup representation is shown in Fig. 4 (b). A well-controlled distance between the in- and output fibers and the GCs is ensured. The coupling angle is fixed at 14°; therefore, the structures coupling spectra have a maximum at different wavelengths (cf. Eq. (1)). The evaluation for each structure will be made at its maximal transmission wavelength. The fixed measurement conditions are needed to guarantee for a stable experimental environment. A calibration measurement supports the proper result normalization and no waveguide loss had to be extracted from the results. The given values of coupling loss and 3σ deviation are rounded up to the first decimal place.

Results and discussion

In this section, we summarize the most important results of our numerical and experimental analysis on integrated focusing GCs for TM.

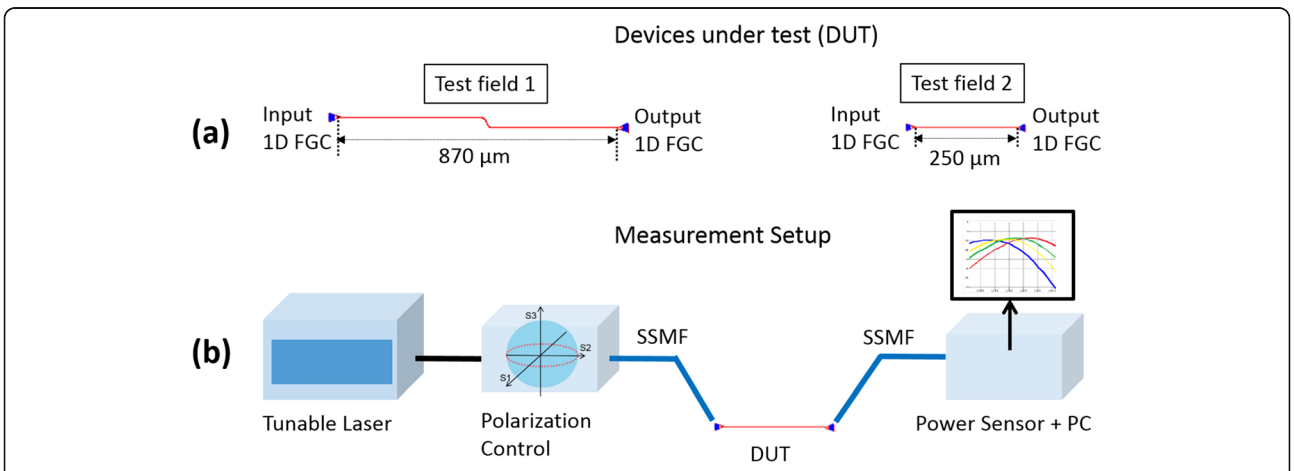

Fig. 4 a Devices under test (DUT) comprising two 1D FGCs at the in- and outputs, connected by a short waveguide. Test field 1 has a waveguide length of 870 μm; test field 2 has a waveguide length of 250 μm. **b** Experimental setup for the FGC back-to-back characterization, including a laser source, a polarization controller, standard single-mode-fibers (SSMF) for in-and out-coupling and a power sensor

A) Simulation Results

Here, simulation results for wire TM FGCs with different design angles and for rib TM FGCs with different slab heights are presented.

Nanowire focusing TM GC

The grating out-coupled power is found to be maximal for a slot width of 520 nm and an etch depth of 70 nm. For these slot dimensions, two different grating periods for two coupling angles at 1550 nm are chosen – 1 μm for 20° and 940 nm for 13°. Figure 5 (a) shows the simulated coupling loss spectra for both structures. As the automatic measurements are performed at a fixed angle of 14°, the coupling loss of both designs is evaluated for this angle as well (Fig. 5 (b)).

Both structures show a minimal coupling loss of – 4 dB at 1550 nm for their design angles, as can be seen from the coupling spectra maximum in Fig. 5 (a). At 14°, the first design is shifted to the L-band, showing a minimal coupling loss of – 3.8 dB at 1610 nm. The second design is shifted to 1542 nm with no change of the maximal transmission (see Fig. 5 (b)).

Rib-waveguide focusing TM GC

Two different models are used to represent appropriately the geometry and the different stack configurations of a shallowly and deeply etched rib TM FGC. For both GCs, the slot etch depth remains 70 nm, whereas the optimal slot width changes to 480 nm. The grating period is chosen to be 920 nm and is the same for both waveguide types, which makes it possible to see the effect of the slab height variation. With these parameters, the d-rib TM FGC has a coupling angle of 13.5° and the s-rib one 14.3°. The coupling loss spectra shown in Fig. 6 are evaluated at 14° and predict a minimal coupling loss of – 4 dB at 1550 nm for the shallowly etched waveguide (s-rib, 150 nm slab) and – 4.4 dB at 1558 nm for the deeply etched one (d-rib, 100 nm slab). The minimally better behavior of the s-rib TM FGC is not necessarily a general property and may change, if another coupling angle and geometry are chosen.

B) Experimental Results

In this subsection, we show results from large-scale tests on the structures, fabricated in a full photonic BiCMOS flow [18].

Nanowire focusing TM GC

First, the nanowire focusing TM GC with a period of 1 μm is characterized on the first test field. Any differences in terms of maximal transmission wavelength or minimal coupling loss from the previously reported measurement in [22] may be a result of the limited accuracy of the manual angle adjustment and the fact that for the manual measurements, only one chip out of 91 was characterized. The manual single-chip measurement was explicitly performed, in order to control the numerical results and does not represent the statistical behavior on the wafer.

For the wafer mapping, the mean maximum transmission wavelength is determined and used for the characterization of the mean insertion loss. Because of the fixed coupling angle of 14°, the resulting evaluation wavelength for the TM GC is 1625 and for the TE GC – 1552 nm. Figure 7 (a) and (b) shows the wafer map and the histogram with the coupling loss statistics of the TM GCs and Fig. 8 (a) and (b) – of the TE GCs. Statistically, we obtain for the first wire TM FGC a mean loss of – 3.9 dB, which is only 0.1 dB higher than predicted by the simulations. Furthermore, the 3σ interval is only ±0.3 dB, which shows a remarkable robustness against variations on the wafer. By comparison, the TE FGC has indeed a lower mean coupling loss of – 3.2 dB, but also a 3 times larger variation with a 3σ interval of ±0.9 dB. A compensation of the gap between TE and TM in terms of efficiency is possible to some extent by apodizing the

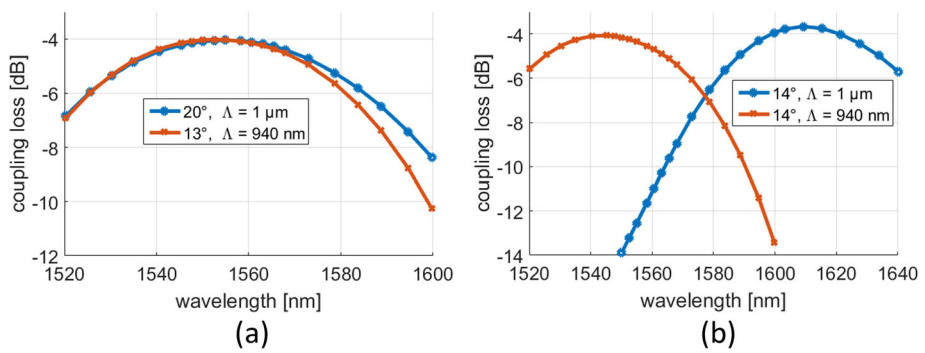

Fig. 5 Simulated coupling loss spectra for nanowire focusing TM GC with different periods Λ, resp. coupling angles: (**a**) evaluation at the design angles, (**b**) evaluation at 14° as a reference to the automatic measurement results

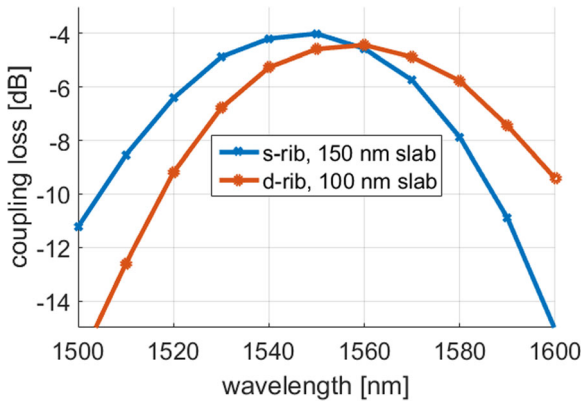

Fig. 6 Simulated coupling loss spectra for a rib-waveguide GCs for TM with two different rib slab heights: shallowly etched (s-rib, 150 nm slab) and deeply etched (d-rib, 100 nm slab). The coupling angle is 14°

TM GC (cf. [14, 15]). The adoption of TM for certain on-chip applications can be a key for reproducible designs and robust large-scale fabrication, as the TM mode with a lower index contrast is less sensitive to process variations.

On the second test field, the second wire TM FGC with a period of 940 nm is characterized for three slot width (w_{slot}) variations – 425 nm, 470 nm and 520 nm (design slot width). The results are summarized in Tab.1. We again obtain a maximal 3σ variation of ±0.3 dB, which confirms that the stability of the wire TM FGCs is repeatable on different test fields.

Exemplary coupling loss spectra of all four wire TM FGCs are shown in Fig. 9 for comparison with the rib waveguide designs. Independent of the existence of an S-bend (the case with period of 1 μm), we see for all structures nearly identical curve shapes with a similar 1 dB bandwidth (45 nm - 47 nm) and no oscillations. Therefore, we can assume that no TM_{00}-TE_{10} conversion takes place.

Rib waveguide focusing TM GC

In the case of rib waveguides, we compare again the performance of TE and TM FGC for each slab height. We first evaluate the FGCs for TE and find little difference in the mean performance of both structures. The s-rib TE FGC (slab 150 nm) shows a mean loss of – 3.8 dB and a 3σ interval of ±0.7 dB at 1515 nm and outperforms only little the d-rib TE FGC (slab 100 nm). The latter has a mean loss of – 3.9 dB a 3σ interval of ±0.8 dB at 1516 nm. Unfortunately, a meaningful comparison with their TM counterparts proves to be difficult, because of an effect occurring in the TM structures, which is expressed in a wavy spectrum shape. Figure 10 (a) and (b) show exemplary this effect, by comparing the coupling loss spectra of TE and TM on a single chip. While for TE we see typical GC curves, the TM have a transmission drop at certain wavelengths resulting in curve oscillations, which make it difficult to define a maximal transmission wavelength and thus a mean loss and a 3σ deviation. The effect seems to be more pronounced for the s-rib TM FGCs, but for d-rib TM FGCs, the dips are

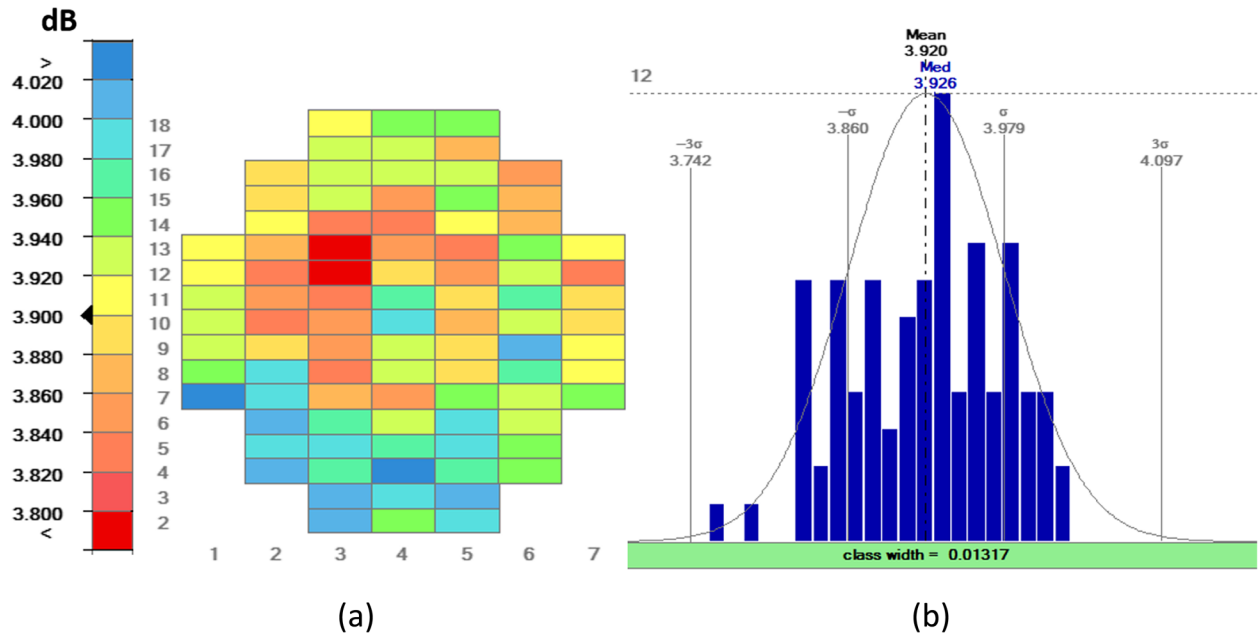

Fig. 7 Wafer map (**a**) and histogram (**b**) for the insertion loss of a wire TM FGC from the first test field. The evaluation wavelength is 1625 nm. The mean coupling loss is – 3.9 dB and the 3σ interval is ±0.3 dB

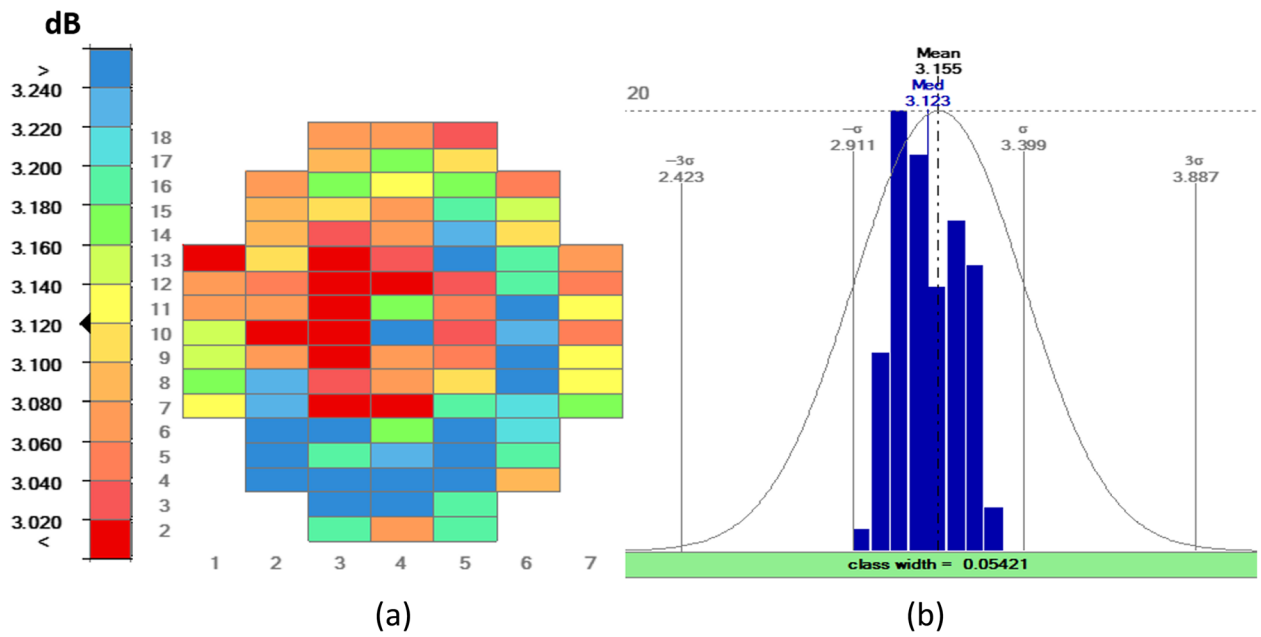

Fig. 8 Wafer map (**a**) and histogram (**b**) for the insertion loss of a wire TE FGC from the first test field. The evaluation wavelength is 1552 nm. The mean coupling loss is − 3.2 dB and the 3σ interval is ±0.9 dB

often at the wavelength where the maximal transmission is expected.

We analyzed possible reasons for the oscillations in the rib TM coupling spectra. As this problem does not occur for rib TE FGCs, we exclude the reason to be the sidewall roughness, as TE should be affected by this problem as well. The typical problem of TM_{00} to TE_{10} conversion is less probable, as the wire TM FGC have the same taper geometry and do not show such oscillations in their spectra (cf. Figure 9). For the same reason, substrate losses are also a less probable reason. A possible explanation for the behavior of the rib structures is a rather rarely reported phenomenon – the TM lateral leakage loss, which was first shown both numerically and experimentally for millimeter waves and later at optical frequencies [29, 30]. In a more recent publication, an experimental demonstration was carried out also on a silicon photonic platform [31]. The reason why this effect could not be seen in the grating coupler simulations is that only the fundamental TM mode is taken into account there and any other modes are usually absorbed by the excitation port.

The lateral leakage loss is caused by a rib TM mode coupling to a TE slab mode at the rib waveguide edge. The following points summarize the theory explained in more detail in the references [29–31]:

– The coupling is not connected to a surface or sidewall roughness, but results, when a guided TM mode fulfils a phase condition allowing it to get leaky.

Table 1 Mean loss and 3σ variation of a wire TM FGCs with a period of 940 nm, an etch depth of 70 nm and varying slot widths. The results are averaged over 61 chips on the same wafer

Slot width	Wavelength	Mean loss	3σ deviation
425 nm	1565 nm	−4.3 dB	± 0.2 dB
470 nm	1550 nm	−4.1 dB	± 0.3 dB
520 nm	1535 nm	− 4.2 dB	± 0.3 dB

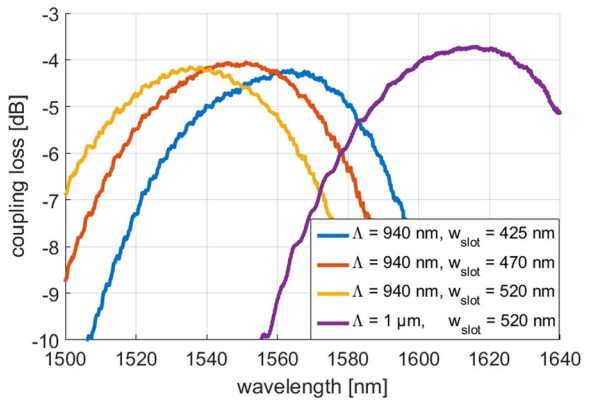

Fig. 9 Exemplary experimental coupling loss spectra of wire TM FGCs with different periods Λ (940 nm or 1 µm) and slot widths w_{slot} measured at 14°

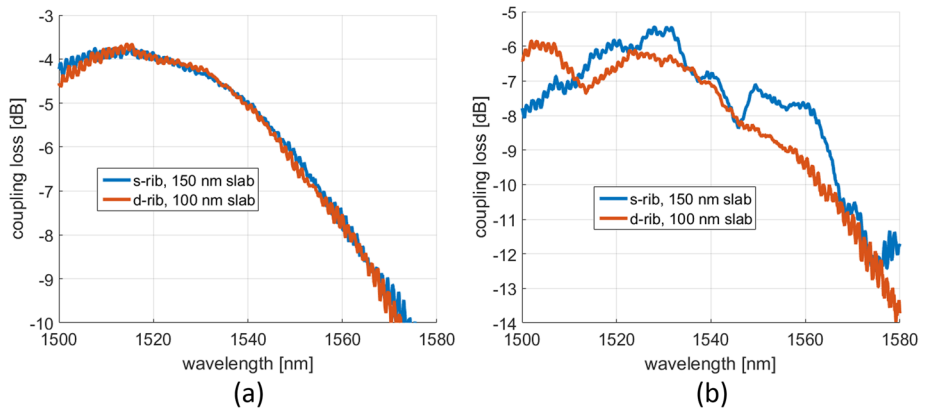

Fig. 10 Exemplary experimental coupling loss spectra of TE (**a**) and TM (**b**) rib FGCs for different slab heights – a shallowly etched (s-rib) waveguide with a slab height of 150 nm and a deeply etched (d-rib) waveguide with a slab height of 100 nm. The coupling angle is 14°

- A mode is completely guided, when the surface waves resulting during its propagation are evanescent in the outer region. Otherwise, the guided mode gets leaky.
- In standard SOI rib waveguides, the fundamental TE mode does not leak, whereas the fundamental TM mode may do. Basically, a guided rib TM mode may leak, when its effective refractive index is lower than those of a TE mode in the slab area.
- The TM lateral leakage loss can be avoided, if the slab height would be sufficiently small. This is a natural convergence to the TM behavior in a wire waveguide.

To investigate if the rib TM mode leaks, a planar dispersion diagram can be used [30]. Here, the effective refractive indices of the two lowest slab waves are plotted depending on the slab height. To obtain the dispersion characteristics of the slab modes, we performed a simulation of a waveguide with a very large width (50 μm) and silicon thickness from 50 nm to 220 nm. The effective refractive indices are calculated at a constant wavelength of 1550 nm with a commercial finite-difference method mode solver by Photon Design. The model takes into account the specifics of the BiCMOS layer stack that covers the waveguide. The numerical results are shown in Fig. 11.

Two specific thicknesses in this diagram are of importance – t_1 corresponding to the thicker rib region and t_2 corresponding to the rib waveguide slab height. A leakage does not occur, when the effective refractive index of the certain mode $n_{eff,TE/TM}$ at the Si thickness t_1 is larger than the effective refractive index of the other mode at t_2 (see Ref. [30], p.8). In our case, the value of t_1 is fixed to be 220 nm. We see that $n_{eff,TE}(t_1)$ is larger than $n_{eff,TM}(t_2)$ for all values of t_2, which confirms that TE rib mode is generally not leaky. In the opposite, $n_{eff,TM}(t_1)$ has smaller values than $n_{eff,TE}(t_2)$ for all slab heights larger than 90 nm. The vertical gray line can be seen as the upper limit of the rib slab height, after which the TM mode becomes leaky.

Obviously, both the shallowly and the deeply etched rib waveguides lie above this line and the gap between the two n_{eff} values (shown with the black arrows) increases with increasing slab height, which is also stated in the literature (e.g. [31]). The wavier spectrum of the s-rib TM FGC may be therefore explained by its higher sensitivity to TM lateral leakage loss. It is evident that if we aim to design rib waveguides for TM, the rib slab height should be below 90 nm. Note that this is a single-wavelength simulation, so if we want to avoid leakage also for longer wavelengths, even lower slab height may be necessary. For the proper function of the lateral pin diode, which is necessary for FWM applications, a slab

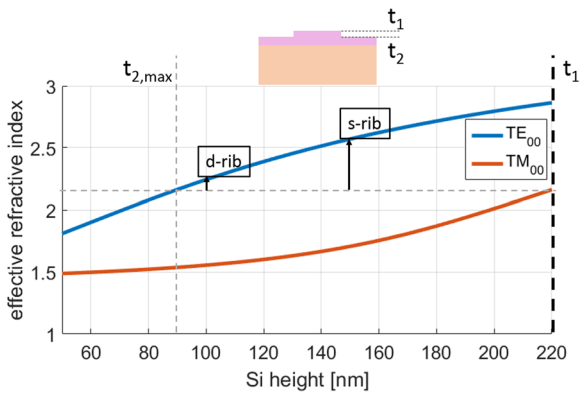

Fig. 11 Effective refractive indices of the fundamental TE and TM modes in a slab waveguide, in dependence on the waveguide height at 1550 nm wavelength. A TM leakage is possible for all rib slab heights, where $n_{eff,TM}(t_1) < n_{eff,TE}(t_2)$ (right from the vertical gray line). Both shallowly etched (s-rib) and deeply etched (d-rib) waveguides find themselves in this area

height of 50 nm is eligible [32]. Therefore, we are still able to design proper rib waveguides for TM for such applications without the effect of a lateral leakage loss. In future, further structures are to be investigated in more detail and tested experimentally.

Conclusion

We designed, fabricated and analyzed numerically and experimentally focusing grating couplers for the fundamental TM_{00} mode, integrated in a photonic BiCMOS platform. The test structures, which are realized in a full photonic BiCMOS flow, are covered by the complete backend-of-line stack. Full-wafer measurements serve to guarantee for their performance under the foundry boundary conditions.

The coupling structures are intended for three types of waveguides – a nanowire, a shallowly etched and a deeply etched rib waveguide. The focusing TM grating couplers for a nanowire show a robust performance and independent of the grating period or slot width a 3σ variation of no more than ±0.3 dB is measured on two separate test fields. Compared to their TE counterparts, the variation on the wafer is three times lower. For the best TM focusing grating coupler design, a mean minimal coupling loss of – 3.9 dB can be achieved.

The characterization of the focusing TM grating coupler design for rib waveguides reveals a possible waveguide design issue. The measured wavy spectra for both shallowly and deeply etched rib TM grating couplers can be caused by a lateral leakage loss. Simulations at 1550 nm wavelength show that the lateral leakage loss can be avoided when the rib slab height is reduced to below 90 nm.

As many of the applications of TM allow the usage of nanowire waveguides, its excitation via focusing grating coupler on a BiCMOS platform proves generally to be reliable, as designs are repeatable and provide enough coupling efficiency. For applications requiring rib waveguides, more care must be taken about the waveguide design itself, in order to guarantee for a smooth performance.

Abbreviations

(Bi)CMOS: (bipolar) Complementary metal-oxide-semiconductor; TE: Transverse electric; TM: Transverse-magnetic; FWM: Four-wave mixing; SMF: Single-mode fiber; GC: Grating coupler; FGC: Focusing grating coupler; s-rib: Shallowly etched rib; d-rib: Deeply etched rib; HBT: Heterojunction bipolar transistor; PML: Perfectly matched layers

Acknowledgements

The authors gratefully acknowledge Prof. Klaus Petermann for valuable discussions on the rib waveguide behavior.

Authors' contributions

Galina Georgieva – numerical analysis and design of the grating couplers; evaluation of measurement data; preparation of the manuscript. Karsten Voigt – numerical modeling and analysis of the rib waveguide designs. Anna Peczek – wafer measurements and preparation of wafer maps and statistics. Christian Mai – fabrication of test structures. Lars Zimmermann – evaluation of photonic BiCMOS integration; large-scale behavior analysis; evaluation of proposed design improvement; edition of the manuscript. The authors read and approved the final manuscript.

Funding

We acknowledge support by the German Research Foundation and the Open Access Publication Fund of TU Berlin.

Availability of data and materials

The datasets used and/or analyzed during the current study are available from the corresponding author on reasonable request.

Competing interests

The authors declare that they have no competing interests.

Author details

[1]Technische Universität Berlin, Office HFT 4, Einsteinufer 25, 10587 Berlin, Germany. [2]IHP – Solutions GmbH, Im Technologiepark 25, 15236 Frankfurt (Oder), Germany. [3]IHP – Leibnitz Institut für innovative Mikroelektronik, Im Technologiepark 25, 15236 Frankfurt (Oder), Germany.

Received: 4 November 2019 Accepted: 22 January 2020
Published online: 08 April 2020

References

1. Mekis, A., et al.: A CMOS Photonics Platform for High-Speed Optical Interconnects, IEEE Photonics Conference 2012, pp. 356–357. Burlingame, CA (2012)
2. Zimmermann, L., et al.: BiCMOS Silicon Photonics Platform, In: Optical Fiber Communication Conference, OSA Technical Digest (online) (Optical Society of America, 2015), paper Th4E.5
3. Yamada, K., et al.: In Guided Light in Silicon-Based Materials. In: Vivien, L., Pavesi, L. (eds). Handbook of Silicon Photonics Series in Optics and Optoelectronics, p. 55. CRC Press (2013)
4. Wang, J., Yao, Z., Lei, T., Poon, A.W.: Silicon coupled-resonator optical-waveguide-based biosensors using light-scattering pattern recognition with pixelized mode-field-intensity distributions. Sci Rep. **4**, 7528 (2014). https://doi.org/10.1038/srep07528
5. Kim, H., Yu, M.: Cascaded ring resonator-based temperature sensor with simultaneously enhanced sensitivity and range. Opt. Express. **24**, 9501–9510 (2016)
6. Juan-Colás, J., Fraser Krauss, T., Johnson, S.: Real-Time Analysis of Molecular Conformation Using Silicon Electrophotonic Biosensors. *ACS Photonics*. **4**, (2017). https://doi.org/10.1021/acsphotonics.7b00580
7. Green, W.M.J., et al.: Silicon Photonic Gas Sensing, pp. 1–3. 2019 Optical Fiber communications conference and exhibition (OFC), San Diego (2019)
8. Brasch, V., Lucas, E., Jost, J.D., Geiselmann, M., Kippenberg, T.: Self-referenced photonic chip soliton Kerr frequency comb. Light Sci Appl. **6**, e16202 (2016). https://doi.org/10.1038/lsa.2016.202
9. Salem, R., Foster, M.A., Turner, A.C., Geraghty, D.F., Lipson, M., Gaeta, A.: Signal regeneration using low-power four-wave mixing on silicon chip. Nat Photonics. **2**, 35–38 (2007). https://doi.org/10.1038/nphoton.2007.249
10. Signorini, S., et al.: Intermodal four-wave mixing in silicon waveguides. Photon Res. **6**, 805–814 (2018)
11. Pintus, P., Huang, D., Morton, P., Shoji, Y., Mizumoto, T., Bowers, J.E.: Integrated Optical Isolator and Circulator in Silicon Photonics, 2018 European conference on optical communication (ECOC), pp. 1–3. Rome (2018)
12. Larrea-Luzuriaga, R.A., Gutiérrez, A.M., Sanchis, P.: Analytical strategy to achieve optimized grating couplers with high precision for both TE and TM polarizations on SOI platform. 2016 IEEE Ecuador Technical Chapters Meeting (ETCM). **01**, 1–5 (2016)
13. Dai, D., Zhang, M.: Mode hybridization and conversion in silicon-on-insulator nanowires with angled sidewalls. Opt Express. **23**, 32452–32464 (2015)
14. Wang, Y., et al.: Focusing sub-wavelength grating couplers with low back reflections for rapid prototyping of silicon photonic circuits. Opt Express. **22**, 20652–20662 (2014)
15. Wang, Y., et al.: Apodized Focusing Fully Etched Subwavelength Grating Couplers. in IEEE Photonics J. **7**(3), 1–10, Art no. 2400110 (2015)
16. Zou, J., Zhang, Y., Hu, J., Wang, C., Zhang, M., Le, Z.: Grating coupler with reduced Back reflection using λ/4 offset at its grating sub-teeth. J. Lightwave Technol. **37**, 1195–1199 (2019)

17. Hoffmann, J., Schulz, M.K., Pitruzzello, G., Fohrmann, L., Petrov, A., Eich, M.: Backscattering design for a focusing grating coupler with fully etched slots for transverse magnetic modes. Sci Rep. **8**, (2018). https://doi.org/10.1038/s41598-018-36082-z
18. Knoll, D., et al.: BiCMOS Silicon Photonics Platform for Fabrication of High-Bandwidth Electronic-Photonic Integrated Circuits, pp. 46–49. 2016 IEEE 16th Topical Meeting on Silicon Monolithic Integrated Circuits in RF Systems (SiRF), Austin (2016)
19. Gajda, A., Zimmermann, L., Bruns, J., Tillack, B., Petermann, K.: Design rules for p-i-n diode carriers sweeping in nano-rib waveguides on SOI. Opt Express. **19**, 9915–9922 (2011)
20. J. Fujikata, T. Nakamura, M. Noguchi and S. Takahashi, "High-Efficiency of Narrow-Width MOS Capacitor Type Si Optical Modulator with TM Mode Excitation," 2019 IEEE 16th international conference on group IV photonics (GFP), Singapore, 2019, pp. 1–2
21. Banakar, M., et al.: High Speed Silicon Capacitor Modulators for TM Polarisation, vol. 2019, pp. 1–2. IEEE 16th international conference on group IV photonics (GFP), Singapore (2019)
22. Georgieva, G., Voigt, K., Zimmermann, L.: Focusing 1D Silicon Photonic Grating Coupler in Photonic BiCMOS Technology for the Excitation of the Fundamental TM Mode. In: 2019 PhotonIcs & Electromagnetics Research Symposium - Spring (PIERS-Spring), pp. 1667-1673. Rome (2019)
23. Taillaert, D.: Grating couplers as interface between optical fibres and nanophotonic waveguides. PhD thesis, Ghent University, Ghent (2004)
24. Chen, X., Tsang, H.K.: Nanoholes grating couplers for coupling between silicon-on-insulator waveguides and optical fibers. in IEEE Photonics J. **1**(3), 184–190 (2009)
25. Booker, H.G., Clemmow, P.C.: The concept of an angular spectrum of plane waves, and its relation to that of polar diagram and aperture distribution. in Proceedings of the IEE - Part III: Radio and Commun Eng. **97**(45), 11–17 (1950)
26. Ura, S., et al.: Focusing grating couplers for polarization detection. J. Lightwave Technol. **6**(6), 1028–1033 (1988)
27. Gedney, S.D.: an Anisotropic PML Absorbing Media for the FDTD Simulation of Fields in Lossy and Dispersive Media. Electromagnetics. **16**(4), 399–415 (1996)
28. Weiland, T.: A discretization method for the solution of Maxwell's equations for six-component fields. Archiv Elektronik und Uebertragungstechnik. **31**, 116–120 (1977)
29. Ogusu, K., Tanaka, I.: Optical strip waveguide: an experiment. Appl Opt. **19**, 3322–3325 (1980)
30. Oliner, A.A., Peng, S., Hsu, T., Sanchez, A.: Guidance and leakage properties of a class of open dielectric waveguides: part II - new physical effects. IEEE Trans Microw Theory Tech. **29**(9), 855–869 (1981)
31. Webster, M.A., Pafchek, R.M., Mitchell, A., Koch, T.L.: Width Dependence of Inherent TM-Mode Lateral Leakage Loss in Silicon-On-Insulator Ridge Waveguides. in IEEE Photonics Technol Lett. **19**(6), 429–431 (2007)
32. Tian, H., et al.: Fabrication of low-loss SOI nano-waveguides including BEOL processes for nonlinear applications. J Eur Optical Soc. **7**, (2012), 12032-1–12032-6

Publisher's Note